Applied Physics Letters ARTICLE pubs.aip.org/aip/apl

Spin-selective nonlinear imaging in real and Fourier space via chiral metasurfaces

Cite as: Appl. Phys. Lett. **129**, 041703 (2026); doi: 10.1063/5.0342546
Submitted: 7 May 2026 · Accepted: 10 July 2026 ·
Published Online: 28 July 2026

Yanchun Wang,[1] Yuebian Zhang,[1,a)] Yuexin Sun,[1] Haoyu Wang,[1] Wenwei Liu,[1] Hua Cheng,[1,b)] and Shuqi Chen[1,2,3,c)]

AFFILIATIONS

[1]The Key Laboratory of Weak Light Nonlinear Photonics, Ministry of Education, School of Physics, TEDA Institute of Applied Physics, Nankai University, Tianjin 300071, China
[2]School of Materials Science and Engineering, Nankai University, Tianjin 300350, China
[3]The Collaborative Innovation Center of Extreme Optics, Shanxi University, Taiyuan, Shanxi 030006, China

[a)]Electronic mail: zhangyb@szlab.ac.cn
[b)]Electronic mail: hcheng@nankai.edu.cn
[c)]Author to whom correspondence should be addressed: schen@nankai.edu.cn

ABSTRACT

Nonlinear chiral metasurfaces represent a compelling platform for spin-selective light–matter interactions and multidimensional optical information processing. However, existing designs are typically restricted to single-parameter manipulation or rely on intricate supercell architectures, making simultaneous and independent control of multiple wavefront degrees of freedom challenging. Here, we present a streamlined design paradigm for nonlinear chiral metasurfaces, in which spin-selective and independent modulation of amplitude and phase can be achieved by adjusting merely two geometric parameters of a single chiral meta-atom. As a proof of concept, we implement a multifunctional metasurface by arranging spatially segregated enantiomeric structures, experimentally demonstrate spin-selective dual-channel nonlinear imaging in real and Fourier space under left- and right-circularly polarized fundamental excitation. Each polarization channel simultaneously generates a near-field grayscale image (real space) and its corresponding far-field holographic reconstruction (Fourier space). This work paves the way toward multifunctional, high-efficiency, and ultracompact nonlinear photonic devices.

Metasurfaces, a planar array composed of artificial subwavelength structures,[1–3] have emerged as powerful platforms for miniaturizing and integrating optical devices by enabling versatile light-field control through precise engineering of individual meta-atoms. In the linear optical regime, metasurfaces have demonstrated remarkable capabilities in wavefront shaping, including focusing,[4,5] anomalous refraction,[6] and holography.[7–9] The recent shift toward multidimensional optical field manipulation has further spawned multifunctional metasurfaces,[10–21] including vectorial holography,[14–16] broadband achromatic metalenses,[17] and optical encryption,[18] significantly expanding their application scope. However, these advances typically rely on multi-element supercell architectures, which not only complicate the fabrication process but also constrain the independent control over multiple optical dimensions within a single pixel. To circumvent these limitations, Li *et al.* proposed an elegant chiral mirror design utilizing a single meta-atom to achieve spin-selective, full-dimensional light manipulation in the linear optical regime,[20] demonstrating the unique advantages of chiral metasurfaces in optical field control.

Extending metasurfaces into the nonlinear optical regime opens new avenues for frequency conversion and wavefront manipulation.[21–38] Benefiting from localized surface plasmon resonances (LSPRs), metallic metasurfaces can dramatically enhance electromagnetic fields at the nanoscale, thereby boosting nonlinear conversion efficiencies.[22–28] Despite this progress, the wavefront shaping capabilities of nonlinear metasurfaces remain largely underdeveloped: existing designs predominantly focus on manipulating a single parameter—either amplitude, phase, or polarization[26,27,29]—while independent and simultaneous control of multiple wavefront degrees of freedom remains elusive. Despite recent advances by Deng *et al.* in realizing simultaneous modulation of amplitude, phase, and polarization for second-harmonic generation (SHG) via grayscale lithography,[30] independently tailoring the amplitude and phase of SHG waves in dual circular polarization-addressable

nonlinear channels via enantiomer-dependent spin-selective SHG responses remains less explored. Chiral metasurfaces, which break inversion symmetry and support strong localized electromagnetic resonances, not only significantly enhance SHG efficiency but also enable effective control of nonlinear circular dichroism (CD) through their selective response to circularly polarized light. These features not only introduce an additional degree of freedom for nonlinear wavefront control[31–34] but also underpin critical applications ranging from nonlinear chiral sensing and holography to integrated photonic devices. For instance, exploiting nonlinear geometric phase through tailored orientation distributions of chiral metasurfaces enables the generation of four distinct third-harmonic holograms under left- and right-circularly polarized (LCP and RCP) excitation, each exhibiting pronounced CD.[34] This stands in stark contrast to conventional Pancharatnam–Berry (PB) metasurfaces, which are inherently restricted to generating merely two holograms with the same pattern and opposite circular polarization states.[35] Despite offering increased information capacity compared to conventional metasurfaces, current chiral designs still lack the capability to simultaneously and independently modulate both the amplitude and phase of SHG waves.

Here, we present a streamlined design paradigm for independently and simultaneously modulating both amplitude and phase of spin-selective SHG waves, thereby enabling dual-space nonlinear imaging (real and Fourier domain) via resonant chiral plasmonic metasurfaces. Our architecture employs a metal–insulator–metal (MIM) configuration comprising a ground gold layer, a photoresist (SU8) spacer layer, and a top layer of gold nanostructures. The key innovation lies in utilizing merely two geometric parameters of a single chiral meta-atom to achieve independent modulation of the amplitude and phase of the SHG wave without resorting to complex supercells. Furthermore, by spatially integrating a pair of enantiomeric meta-atoms with opposite spin-selective responses, we enable spin-selective dual-channel imaging across real and Fourier space under LCP and RCP excitation. Experimentally, we demonstrate concurrent grayscale imaging in real space (near field) and holographic imaging in Fourier space (far field), where each polarization channel carries independent information. This work establishes a practical route toward multi-channel information processing, secure optical communications, and dynamic holographic displays in nonlinear optics. Moreover, owing to its structural simplicity and inherent scalability, the proposed platform holds great potential for broader applications in dual-space optical encoding, data storage, and on-chip integration.

The conceptual design of the resonant chiral metasurface for simultaneous amplitude and phase modulation of SHG wave is illustrated in Fig. 1. As shown in Fig. 1(a), the metasurface comprises two types of enantiomeric structures (A and B) with opposite chirality arranged in spatially separated regions. Owing to the intrinsic spin-selective response of chiral meta-atoms, only one enantiomer is selectively excited when illuminated by a specific circularly polarized fundamental wave (FW), thereby enabling spin-selective nonlinear imaging in real and Fourier space: enantiomer A responds exclusively to LCP light, generating a grayscale image in real space (near field, "windmill") and a holographic image in Fourier space (far field, "moon") in the SHG signal, while enantiomer B is activated only by RCP light, producing a windmill with opposite rotation direction in real space and a holographic "star" in Fourier space.

The unit cell geometry is depicted in Fig. 1(b). The metasurface adopts an MIM configuration consisting of a ground gold layer (thickness $h_3 = 100$ nm), an SU8 spacer ($h_2 = 160$ nm), and a top gold nanostructure layer ($h_1 = 30$ nm), with periodicities $P_x = P_y = 510$ nm. The chiral nanostructure features an outer radius $r_1 = 215$ nm, an inner radius $r_2 = 145$ nm, and an arc width $w = 70$ nm. Figure 1(c) details the critical structural variables enabling independent wavefront control. The short-arc length is parameterized by angle α, which governs the amplitude of the SHG wave by tailoring the LSPR strength, while the in-plane rotation angle θ imparts a geometric phase shift for full 2π phase coverage of the SHG wave. The symmetric arc length is fixed at $\beta = 70°$. By judiciously designing the spatial distributions of α and θ across the metasurface, independent modulation of both amplitude and phase of the SHG wave is achieved within a single functional layer.

To investigate the spin-selective behavior of the designed chiral metasurface, we performed finite-element method simulations using the commercial software COMSOL Multiphysics. Periodic boundary conditions were applied in the x and y directions, with perfectly matched layers (PML) in the z direction. The permittivity of gold was taken from Palik's handbook,[39] and the refractive index of SU8 was set to 1.53. Figure 2(a) presents the simulated polarization-resolved linear reflection spectra of periodically arranged enantiomer A resonators. Under LCP excitation, a sharp dip with near-zero reflectance appears at 1525 nm in the LCP–LCP channel, whereas the RCP–RCP reflectance remains above 0.6, demonstrating strong spin-selective

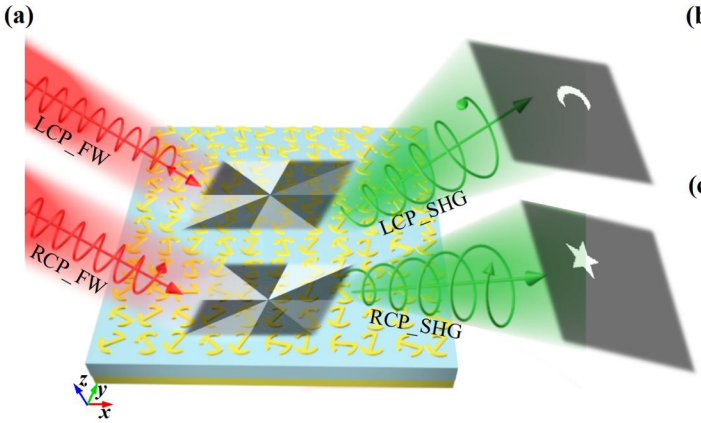

FIG. 1. Design schematic of the resonant chiral plasmonic metasurface. (a) Spin-selective nonlinear imaging in real space (grayscale imaging) and Fourier space (holographic imaging) under LCP and RCP FW excitation. (b) Unit cell geometry showing the metal–insulator–metal (MIM) configuration. (c) Structural variables defining the chiral meta-atom: α (short-arc length) predominantly governs the amplitude of SHG wave, while θ (in-plane rotation) predominantly controls the phase of SHG wave.

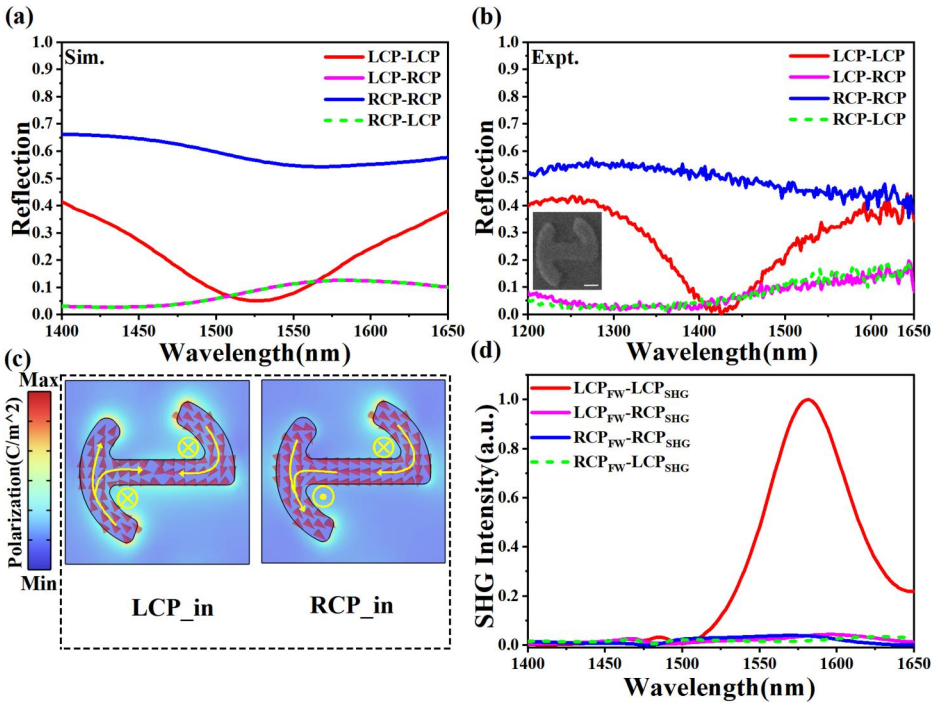

FIG. 2. Linear and nonlinear optical characterization of the chiral metasurface. (a) Simulated and (b) measured linear reflection spectra of enantiomer A under circularly polarized illumination, showing co-polarized (LCP–LCP, RCP–RCP) and cross-polarized (LCP–RCP, RCP–LCP) components. Inset: SEM image of the fabricated enantiomer A ($\theta = 0°$, $\alpha = 50°$). Scale bar: 100 nm. (c) Surface current distributions (red arrows) and power loss density maps at the fundamental wavelength of 1525 nm, illustrating the spin-selective resonance mechanism under LCP and RCP excitation. (d) Simulated SHG reflection spectra under LCP and RCP FW excitation, displaying the power ratio of reflected SHG to incident FW, LCP_{FW}–LCP_{SHG} is defined as the ratio of the power of the reflected SHG LCP component to that of the incident FW LCP wave.

reflection. Considering fabrication constraints, we use structures with rounded corners in the simulations. The experimentally measured spectra in Fig. 2(b) confirm this trend, exhibiting an overall blueshift attributed to fabrication-induced corner rounding and dimensional deviations. Simulations confirm that increasing corner rounding systematically blueshifts the resonance. Enantiomer B, obtained by rotating enantiomer A 180° around the y axis, exhibits the opposite spin-selective spectral response.

We further revealed the physical origins of spin selectivity by analyzing the surface current distributions of enantiomer A at the fundamental resonance. As shown in Fig. 2(c), LCP excitation induces antiparallel electric dipoles (indicated by red arrows) that generate parallel magnetic dipoles along the propagation direction, establishing a magnetic dipole resonance that traps energy within the structure and produces the observed reflection dip. Conversely, RCP excitation creates parallel electric dipoles with antiparallel magnetic moments that destructively interfere, suppressing field localization and yielding high reflection. This distinct near-field behavior underpins the chiral metasurface's ability to selectively enhance electromagnetic fields for specific spin states. Figure 2(d) presents the nonlinear optical response calculated using a hydrodynamic model.[36] The strongest SHG signal occurs at 1582 nm under LCP excitation—approximately 57 nm redshifted from the fundamental resonance. This offset arises from field localization at the structure edges: sharp geometries concentrate fields at tips, whereas rounded corners (adopted here to match fabrication realities) redistribute the field distribution and modify the resonant coupling conditions. Consequently, the SHG peak and linear resonance occur at distinct wavelengths, with the localized fundamental fields at 1582 nm providing the necessary enhancement for efficient nonlinear wavefront manipulation.

To realize fully independent modulation of amplitude and phase, we systematically investigated the SHG wave radiation properties of enantiomer A under LCP excitation (enantiomer B exhibits analogous behavior under RCP). With the symmetric arc angle β fixed at 70°, we varied the short-arc length $\alpha\,(40° - 85°)$ to tailor the localized plasmonic resonance—thereby modulating the amplitude of SHG wave—while scanning the orientation angle $\theta\,(0° - 180°)$ to control the phase. Figures 3(a) and 3(b) map the normalized amplitude and phase distributions of the SHG wave, respectively, across this two-dimensional parameter space. Four discrete amplitude levels—A1 (0.28), A2 (0.55), A3 (0.79), and A4 (1.0)—were extracted from the amplitude contours [dashed lines in Fig. 3(a)]. For each level, five specific meta-atoms were selected to provide uniform phase coverage from $-\pi$ to π while maintaining nearly constant amplitude, as validated by the averaged profiles in Fig. 3(c) (amplitude stability) and Fig. 3(d) (linear phase progression). This strategy achieves independent quantization of both amplitude and phase within a single meta-atom. The phase modulation originates from the combined effect of geometric phase and resonant phase. According to the nonlinear selection rules for onefold (C1) symmetric meta-atoms under LCP excitation,[28] the reflected SHG wave (LCP channel) carries a phase term of 3θ. Consequently, rotating the structure by approximately 120° yields the requisite 2π phase shift, consistent with the continuous phase variation shown in Fig. 3(b). The apparent phase jumps arise from phase wrapping within the $-\pi$ to π range. It is worth noting that varying the structural parameter α modifies the geometry of the meta-atom and its local resonant response, and, therefore, may affect both the amplitude and phase of the SHG wave. Based on this consideration, α and θ are not treated as strictly decoupled control variables for the amplitude and phase. Instead, the structural parameter combinations are selected from numerically simulated two-dimensional

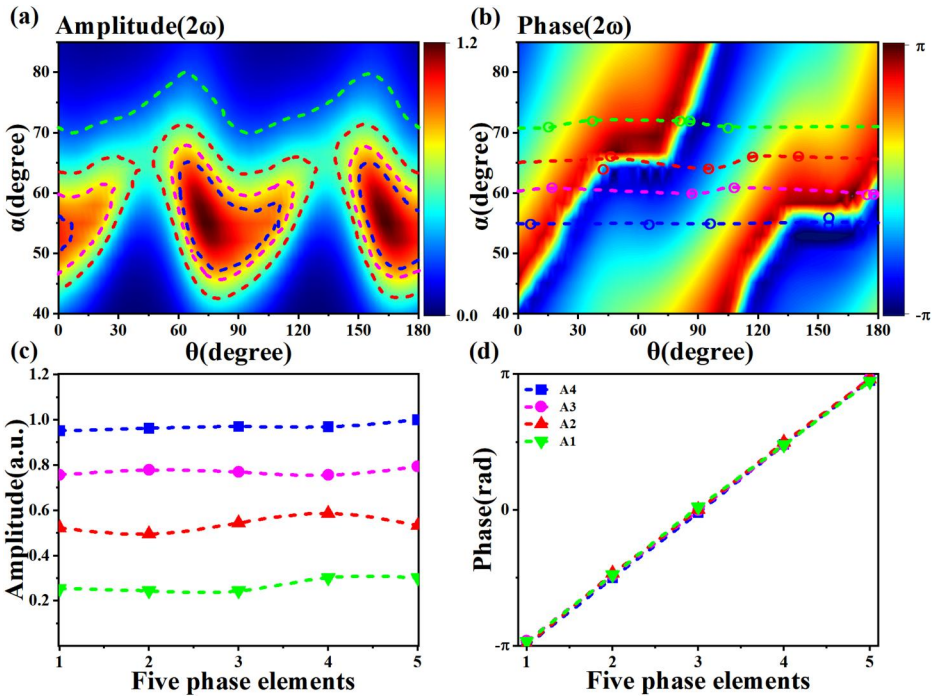

FIG. 3. Parametric design space for phase and multi-level amplitude modulation of SHG wave for enantiomer A under LCP excitation (LCP–LCP channel). Normalized SHG (a) amplitude and (b) phase as functions of the short-arc length (α) and rotation angle (θ). The dashed contours indicate four amplitude levels (A1 = 0.28, A2 = 0.55, A3 = 0.79, and A4 = 1.0), while the colored markers denote structural parameters providing phase shifts of $-\pi$, $-\pi/2$, 0, $\pi/2$, and π at each amplitude level. (c) Averaged SH amplitude and (d) accumulated phase for the selected five-phase-element groups within each amplitude level, demonstrating discrete yet uniform phase progression across the full 2π range with nearly constant amplitude maintenance.

amplitude–phase response maps to simultaneously meet the target amplitude and phase requirements, thereby realizing the desired independent amplitude and phase distributions while taking into account the actual parameter-dependent response of the meta-atoms.

We experimentally validated the spin-selective independent modulation of amplitude and phase in the chiral metasurface by demonstrating spin-selective nonlinear imaging in dual-space under a 1480 nm FW excitation, as shown in Fig. 4. The nonlinear optical response of the chiral metasurface was characterized using a home-built far-field nonlinear optical microscopy system. The incident FW was generated from an optical parametric oscillator (OPO) pumped by a mode-locked Yb:KGW femtosecond laser oscillator (FLINT FL1, Light Conversion; repetition rate: 76 MHz). The OPO output was converted into LCP or RCP light using a linear polarizer (LP) and a

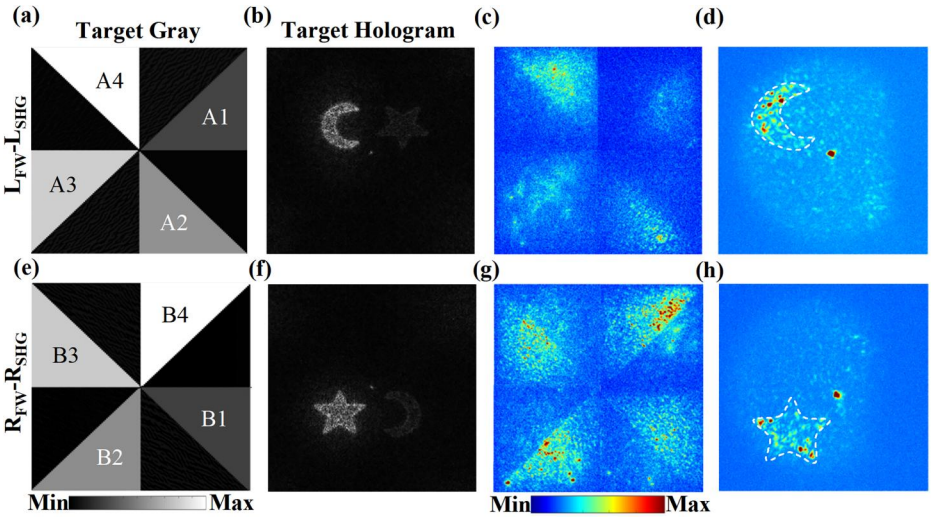

FIG. 4. Experimental demonstration of spin-selective nonlinear imaging in real and Fourier space. (a) and (b) Target grayscale image in real space (near field, four-level windmill) and hologram reconstruction in Fourier space (far field, moon) for LCP FW excitation. The designed image has dimensions of 280 × 280 pixels, with each pixel consisting of a single unit cell. (c) and (d) corresponding experimental results. The white dotted lines outline the edges of the pattern. (e) and (f) Target patterns and (g) and (h) measured results for RCP excitation, yielding an opposite rotating windmill grayscale pattern in real space and a star hologram in Fourier space. Designed intensity ratios: A1 = 0.28, A2 = 0.55, A3 = 0.79, and A4 = 1.0 (B1–B4 correspond to A1–A4 with inverted contrast).

quarter-wave plate (QWP), expanded by a beam expander, and focused onto the chiral metasurface sample with a 20× objective (NA = 0.45). The back-reflected SHG signal was collected by the same objective and separated from the residual FW by a beam splitter. After passing through a relay lens (f = 150 mm), a short-pass filter, a QWP, and an LP, the selected LCP or RCP component of the SHG signal was imaged onto an sCMOS camera (HAMAMATSU ORCA-Flash4.0 V3). Each circular polarization channel simultaneously generates a grayscale image in real space and its corresponding holographic reconstruction in Fourier space. The metasurface comprises two types of enantiomeric chiral structures arranged in spatially separated blocks, encoding two target near-field windmill patterns in real space with opposite rotation directions and their respective far-field holograms (moon and star) in Fourier space calculated by the Gerchberg–Saxton algorithm.

In Fig. 4(a), the grayscale pattern comprises four distinct regions, each corresponding to five specific structural parameters of enantiomer A1–A4, while the four dark regions are formed by the complementary enantiomeric structures B1–B4. Under LCP excitation, only the A regions are selectively excited, producing the windmill pattern in real space shown in Fig. 4(c). The measured integral intensity ratio of A1:A2:A3:A4 = 0.29:0.51:0.55:1 confirms the dominance of A-enantiomer response while the B regions remain suppressed, though amplitude deviations reduce the contrast between grayscale levels. Simultaneously, the hologram reconstruction in Fourier space (moon) of the SHG wave can be recognized [Fig. 4(d)], showing an overall correspondence with the calculated target [Fig. 4(b)]. Under RCP excitation, only the B-enantiomer regions are activated, generating a counter-rotating windmill in real space [Fig. 4(e)] pattern and the corresponding star hologram in Fourier space [Fig. 4(f)]. The measured integral intensity of B1:B2:B3:B4 = 0.75:1:0.88:1 [Fig. 4(g)], indicating the selective activation of the B-enantiomer regions under RCP excitation. However, the experimentally obtained grayscale contrast still deviates from the ideal design. This deviation can be attributed to fabrication-induced geometrical variations of the resonant meta-atoms, such as changes in the short-arc length, edge rounding, and feature size. In addition to the amplitude deviation, fabrication-induced resonance shifts can also affect the phase response of the selected meta-atoms. Since the phase of the SHG wave consists of both the nonlinear geometric phase and the resonant phase, changes in the structural geometry and resonance position can modify the resonant phase and cause the total phase to deviate from the designed value. Consequently, the selected phase states may no longer maintain complete 2π phase coverage, introducing phase errors into the holographic phase profile and degrading the Fourier-space reconstruction quality. This accounts for the increased background noise and blurred contours in the reconstructed moon and star holographic images. Owing to the limited beam size, the four-level intensity ratios of the grayscale images were obtained by scanning four sample regions and stitching the effective imaging areas after background subtraction and intensity normalization. Despite these experimental imperfections, the results clearly demonstrate that the chiral metasurface enables spin-selective, independent control of both amplitude and phase for dual-space nonlinear imaging.

In conclusion, we have demonstrated a nonlinear chiral metasurface platform that enables spin-selective dual-space in real and Fourier domains via single-pixel meta-atoms. By introducing two independent geometric degrees of freedom, the short-arc length (α) predominantly governing amplitude and the rotation angle (θ) predominantly governing phase, we thereby circumvent the need for complex supercell architectures. Leveraging this independent control mechanism, we achieve simultaneous yet decoupled modulation of the amplitude and phase of the SHG wave without resorting to complex supercell architectures. To realize spin-addressable dual-space imaging, we spatially integrate enantiomeric chiral structures with opposite spin-selective responses within a single metasurface. This configuration enables spin-selective nonlinear imaging in real and Fourier space under LCP and RCP excitation, where each channel simultaneously projects distinct grayscale patterns in real space and holographic imaging in Fourier space. Experimentally, we validate that each polarization state carries independent information across both domains, confirming the spin-selective nature of our design.

Compared with existing nonlinear metasurfaces limited to single-parameter manipulation or complex supercell designs, our approach uniquely combines structural chirality with minimalist geometric control to simultaneously govern the amplitude and phase of the SHG wave. This significantly extends the accessible degrees of freedom for nonlinear wavefront engineering from single-space to dual-space imaging, while enhancing information capacity and design flexibility. Our work establishes a practical route toward multifunctional, ultracompact nonlinear photonic devices capable of parallel information processing, with immediate applications in polarization-selective wavefront manipulation, optical encryption, secure communications, and integrated nanophotonics.

This work was supported by the National Key Research and Development Program of China (Nos. 2021YFA1400601 and 2024YFA1409903) and the National Natural Science Foundation of China (Nos. 12474331, W2441005, 12192253, 12274237, 12274239, 12534014, 12547181, and U22A20258).

AUTHOR DECLARATIONS

Conflict of Interest

The authors have no conflicts to disclose.

Author Contributions

Yanchun Wang: Conceptualization (lead); Data curation (lead); Formal analysis (equal); Investigation (equal); Methodology (equal); Software (equal); Writing – original draft (lead). **Yuebian Zhang:** Conceptualization (equal); Investigation (equal); Supervision (equal); Writing – review & editing (equal). **Yuexin Sun:** Investigation (supporting); Software (supporting); Validation (equal). **Haoyu Wang:** Investigation (supporting); Validation (equal). **Wenwei Liu:** Investigation (supporting); Visualization (equal). **Hua Cheng:** Conceptualization (equal); Formal analysis (equal); Writing – review & editing (equal). **Shuqi Chen:** Funding acquisition (equal); Project administration (equal); Resources (equal); Supervision (equal); Writing – review & editing (equal).

DATA AVAILABILITY

The data that support the findings of this study are available from the corresponding author upon reasonable request.

REFERENCES

[1]N. Yu, P. Genevet, M. A. Kats, F. Aieta, J.-P. Tetienne, F. Capasso, and Z. Gaburro, Science **334**, 333–337 (2011).
[2]X. Chen, L. Huang, H. Mühlenbernd, G. Li, B. Bai, Q. Tan, G. Jin, C.-W. Qiu, S. Zhang, and T. Zentgraf, Nat. Commun. **3**, 1198 (2012).
[3]N. Yu and F. Capasso, Nat. Mater. **13**, 139–150 (2014).
[4]F. Aieta, P. Genevet, M. A. Kats, N. Yu, R. Blanchard, Z. Gaburro, and F. Capasso, Nano Lett. **12**, 4932–4936 (2012).
[5]M. Khorasaninejad, W. T. Chen, R. C. Devlin, J. Oh, A. Y. Zhu, and F. Capasso, Science **352**, 1190–1194 (2016).
[6]L. Huang, X. Chen, H. Muhlenbernd, G. Li, B. Bai, Q. Tan, G. Jin, T. Zentgraf, and S. Zhang, Nano Lett. **12**, 5750–5755 (2012).
[7]S. Sun, Z. Zhou, C. Zhang, W. Yang, Q. Song, and S. Xiao, Ann. Phys. **530**, 1700418 (2018).
[8]D. Wen, F. Yue, G. Li, G. Zheng, K. Chan, S. Chen, M. Chen, K. F. Li, P. W. H. Wong, K. W. Cheah *et al.*, Nat. Commun. **6**, 8241 (2015).
[9]R. C. Devlin, M. Khorasaninejad, W. T. Chen, J. Oh, and F. Capasso, Proc. Natl. Acad. Sci. U. S. A. **113**, 10473–10478 (2016).
[10]A. Asad, H. S. Khaliq, N. Mahmood, and Y. Massoud, Proc. SPIE **12318**, 27–32 (2022).
[11]A. C. Overvig, S. Shrestha, S. C. Malek, M. Lu, A. Stein, C. Zheng, and N. Yu, Light: Sci. Appl. **8**, 92 (2019).
[12]L. Deng, J. Deng, Z. Guan, J. Tao, Y. Chen, Y. Yang, D. Zhang, J. Tang, Z. Li, Z. Li *et al.*, Light: Sci. Appl. **9**, 101 (2020).
[13]M. Liu, W. Zhu, P. Huo, L. Feng, M. Song, C. Zhang, L. Chen, H. J. Lezec, Y. Lu, A. Agrawal *et al.*, Light: Sci. Appl. **10**, 107 (2021).
[14]Z.-L. Deng, J. Deng, X. Zhuang, S. Wang, K. Li, Y. Wang, Y. Chi, X. Ye, J. Xu, G. P. Wang *et al.*, Nano Lett. **18**, 2885–2892 (2018).
[15]T. Liu, C. Dai, D. Wang, C. T. Chan, and L. Zhou, Adv. Photonics **7**, 056004 (2025).
[16]Z.-L. Deng, M. Jin, X. Ye, S. Wang, T. Shi, J. Deng, N. Mao, Y. Cao, B.-O. Guan, A. Alù *et al.*, Adv. Funct. Mater. **30**, 1910610 (2020).
[17]S. Wang, P. C. Wu, V.-C. Su, Y.-C. Lai, C. Hung Chu, J.-W. Chen, S.-H. Lu, J. Chen, B. Xu, C.-H. Kuan *et al.*, Nat. Commun. **8**, 187 (2017).
[18]X. Zhang, J. Cheng, W. Yue, Z. Li, D.-Y. Choi, Y. Li, H. Li, S.-S. Lee, S. Chen, and S. Gao, Nanophotonics **12**, 3747–3756 (2023).
[19]W. Liu, Z. Li, Z. Li, H. Cheng, C. Tang, J. Li, S. Chen, and J. Tian, Adv. Mater. **31**, 1901729 (2019).
[20]Z. Li, W. Liu, H. Cheng, D.-Y. Choi, S. Chen, and J. Tian, Adv. Mater. **32**, 1907983 (2020).
[21]J. Cheng, Z. Li, D.-Y. Choi, S. Yu, W. Liu, H. Wang, Y. Zhang, H. Cheng, J. Tian, and S. Chen, Adv. Opt. Mater. **11**, 2202329 (2023).
[22]G. Grinblat, Y. Li, M. P. Nielsen, R. F. Oulton, and S. A. Maier, Nano Lett. **16**, 4635–4640 (2016).
[23]A. Fedotova, M. Younesi, J. Sautter, A. Vaskin, F. J. Löchner, M. Steinert, R. Geiss, T. Pertsch, I. Staude, and F. Setzpfandt, Nano Lett. **20**, 8608–8614 (2020).
[24]X. Zhang, J. Deng, M. Jin, Y. Li, N. Mao, Y. Tang, X. Liu, W. Cai, Y. Wang, K. Li *et al.*, Sci. China Phys., Mech. Astron. **64**, 294215 (2021).
[25]Y. Gao, Y. Fan, Y. Wang, W. Yang, Q. Song, and S. Xiao, Nano Lett. **18**, 8054–8061 (2018).
[26]Y. Tang, Y. Intaravanne, J. Deng, K. F. Li, X. Chen, and G. Li, Phys. Rev. Appl. **12**, 024028 (2019).
[27]D. Frese, Q. Wei, Y. Wang, M. Cinchetti, L. Huang, and T. Zentgraf, ACS Photonics **8**, 1013–1019 (2021).
[28]W. Ye, F. Zeuner, X. Li, B. Reineke, S. He, C.-W. Qiu, J. Liu, Y. Wang, S. Zhang, and T. Zentgraf, Nat. Commun. **7**, 11930 (2016).
[29]M. Ma, Z. Li, W. Liu, C. Tang, Z. Li, H. Cheng, J. Li, S. Chen, and J. Tian, Laser Photonics Rev. **13**, 1900045 (2019).
[30]J. Deng, Z. Hu, Y. Chen, J. Chen, H. Wang, K. Li, Y. Kivshar, and G. Li, Nano Lett. **25**, 7450–7456 (2025).
[31]D. Kim, J. Yu, I. Hwang, S. Park, F. Demmerle, G. Boehm, M.-C. Amann, M. A. Belkin, and J. Lee, Nano Lett. **20**, 8032–8039 (2020).
[32]L. Kang, C.-Y. Wang, X. Guo, X. Ni, Z. Liu, and D. H. Werner, Nano Lett. **20**, 2047–2055 (2020).
[33]Y. Jiang, W. Liu, Z. Li, D.-Y. Choi, Y. Zhang, H. Cheng, J. Tian, and S. Chen, Adv. Opt. Mater. **11**, 2202186 (2023).
[34]X. Hong, K. Wang, C. Guan, X. Han, Y. Chen, S. Qian, X. Xing, C.-W. Qiu, and P. Lu, Nano Lett. **22**, 8860–8866 (2022).
[35]N. Mao, J. Deng, X. Zhang, Y. Tang, M. Jin, Y. Li, X. Liu, K. Li, T. Cao, K. Cheah *et al.*, Nano Lett. **20**, 7463–7468 (2020).
[36]Z. Hao, W. Liu, Z. Li, Z. Li, G. Geng, Y. Wang, H. Cheng, H. Ahmed, X. Chen, J. Li *et al.*, Laser Photonics Rev. **15**, 2100207 (2021).
[37]F. Walter, G. Li, C. Meier, S. Zhang, and T. Zentgraf, Nano Lett. **17**, 3171–3175 (2017).
[38]Y. Sun, G. Geng, Y. Wang, Y. Zhang, Z. Li, W. Liu, H. Cheng, and S. Chen, Laser Photonics Rev. **18**, 2300866 (2024).
[39]E. D. Palik, *Handbook of Optical Constants of Solids* (Academic Press, 1998), Vol. 3.